Surface Functionalization with Ni of Fe$_{0.7}$Cr$_{1.3}$O$_3$/8YSZ Electrode in a Potentiometric Sensor To Selectively Detect C$_2$H$_4$

F. Toldra-Reig and J. M. Serra*[ID]

Instituto de Tecnología Química, Universitat Politècnica de València, Consejo Superior de Investigaciones Científicas, Av Naranjos s/n, E-46022 Valencia, Spain

S *Supporting Information*

ABSTRACT: This work presents a multidevice potentiometric sensor consisting of Fe$_{0.7}$Cr$_{1.3}$O$_3$/8YSZ//8YSZ//Pt to detect selectively C$_2$H$_4$ with a low cross-sensitivity to CO in diesel exhaust gases. The device has been designed as a multisensor to measure up to four channels at the same time. A dense 8YSZ disk is employed as oxide-ion conducting electrolyte where four rectangular-shape working electrodes (Fe$_{0.7}$Cr$_{1.3}$O$_3$/8YSZ) are screen-printed in one face while one common cross-shape reference electrode (LSM/8YSZ) is screen printed in the back face. Two major improvements are proposed in this work: first, change the reference electrode from state-of-the-art Pt to LSM/8YSZ, inexpensive and more active to oxygen. And second, increase the catalytic activity of the working electrode to improve the response of the sensor under wet conditions. The surface activation by nickel and ruthenium nanoparticles deposition enables reduction of the cross-sensitivity toward CO even in wet atmospheres. Ni nanoparticles selectively boost the electrochemically driven oxidation to C$_2$H$_4$ with respect to CO oxidation, as inferred by impedance spectroscopy analysis.

KEYWORDS: *hydrocarbon, ethylene, potentiometric, sensor, YSZ, electrochemical cell*
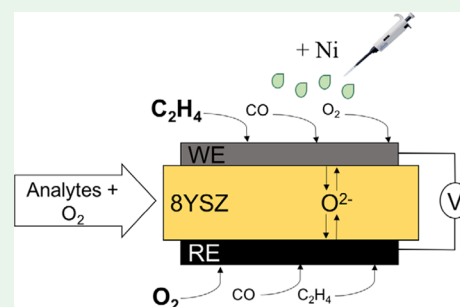
1. INTRODUCTION

Hydrocarbon detection in diesel exhaust gases is getting an increased relevance due to health factors. American, European, and Japanese legislations are more and more restrictive to emission of pollutants that are related to health issues.[1−4] The main problem is the current impossibility to detect such hydrocarbons at lower concentrations. Thus, the development of a sensor able to detect hydrocarbons in atmospheres like exhaust gases will help legislators to keep on pushing for further restrictions in pollutants.

Because of the high temperature of these gases, a potentiometric sensor is the most appropriate type of sensor to perform the detection of hydrocarbons. The sensor works as an ion-based electrochemical cell, where oxygen is reduced on the reference electrode and the generated oxygen ions go through the solid electrolyte (e.g., 8YSZ and CGO) to oxidize the target gas on the working electrode. The advantage of this kind of sensor, apart from temperature, is that working and reference electrodes could be exposed to the same atmosphere. The working electrode should be active to the target compound with low cross-sensitivity to other compounds in the exhaust gas, while the reference electrode should be catalytic active to oxygen. C$_2$H$_4$ is selected as the target gas since it is one of the most abundant hydrocarbons in exhaust gases with a concentration range of 100 ppm (and almost a 30% of the total hydrocarbons) and also exhibits the highest ozone forming potential of all the major hydrocarbon emission sources.[5−8] Nevertheless, other compounds present at the exhaust gases such as water, carbon monoxide (CO), and aromatic compounds must be taken into account. Several perovskites and metal oxides[9−22] are suitable to measure not only hydrocarbons but also other compounds of exhaust gases: CO, NO$_x$, NH$_3$, etc.

In a previous work, a device consisting of Fe$_{0.7}$Cr$_{1.3}$O$_3$/8YSZ//8SZ//Pt that provided a selective response to C$_2$H$_4$ with low cross-sensitivity to CO was reported.[23] However, the addition of water reduces such selectivity to C$_2$H$_4$ and low cross-sensitivity toward CO. In this work, different strategies are proposed to improve the sensor response and its capability. First, a new configuration has been developed to measure several materials. This consists of a solid 8YSZ membrane electrolyte[24,25] with four rectangular working electrodes on the top face and one common reference electrode on the back face. Fe$_{0.7}$Cr$_{1.3}$O$_3$ is selected as working electrode because of its selectivity toward C$_2$H$_4$ and low cross-sensitivity to CO.[26] Second, platinum is usually employed as reference electrode[3,10−12,15−22,27] due to its high catalytic activity while here LSM/8YSZ electrode is employed because of its good ionic conductivity and low price compared to platinum.[28−30] Furthermore, water influence can be critical and affect the device selectivity to C$_2$H$_4$. In this work, the surface of the working electrode is functionalized with nickel and ruthenium to increase the catalytic activity to C$_2$H$_4$ and decrease the influence of water and CO. These elements are selected

because of their good catalytic activity for oxidation of hydrocarbons and CO.[31−34] Adsorption and dissociation of C_2H_4 or CO gas-phase reaction should be promoted to increase the device performance.

The built sensor voltage is measured in atmospheres containing C_2H_4 and CO, as they are the major compounds in an exhaust gas. A constant 6% concentration of O_2 is employed, and the influence of water and aromatics is also studied.

2. EXPERIMENTAL SECTION

2.1. Synthesis of Electrode Materials. The starting materials for the working and reference electrodes were commercial nitrates from Sigma-Aldrich. A sol−gel chemical route was followed to obtain the $La_{0.9}Sr_{0.1}MnO_3$ perovskite (LSM) and $Fe_{0.7}Cr_{1.3}O_3$. Water-based dissolution with the stoichiometric quantities of precursors is obtained. After that, citric acid (Sigma-Aldrich) was added as a chelating agent to prevent partial segregation of the metal components, and ethylene glycol was added to polymerize with the chelating agent and produce an organometallic polymer resin (in a molar ratio 1:2:4 with respect to nitrates solution, citric acid, and ethylene glycol, respectively). This complexation is followed by dehydration at low temperature (up to 200 °C), and finally, thermal decomposition of the precursors at 600 °C led to the formation of nanosized crystalline phases.

Finally, the obtained powders were mixed with 8YSZ powder (Tosoh) in a ball mill for 24 h in a 1:1 volume ratio. This mixture of powders is then mixed with an organic binder (terpineol with a 6 wt % ethylcellulose) in a 1:2 weight ratio and passed through a three-roller mill to obtain screen-printing inks. Previously, the powder was sintered at 1350 °C for 10 h and milled to produce the target crystalline phase and a homogeneous particle size. The structure of the $Fe_{0.7}Cr_{1.3}O_3$ phase in the as-sintered electrode was checked by means of XRD employing a database (ICDD PDF4) to check the crystalline structure (ICDD 00-035-1112).

Since $Fe_{0.7}Cr_{1.3}O_3$ did not attach properly to the 8YSZ electrolyte, $Fe_{0.7}Cr_{1.3}O_3$ and 8YSZ composites were employed to ensure the attachment, which in turn led to an increase of the triple phase boundary surface. This is also desired in the case of LSM as this provides ionic and electronic conductivity in the electrode.

2.2. Fabrication of the Sensor Device. In this work, a multidevice is designed to simultaneously measure four channels (Figure 1). As electrolyte, dense 8YSZ (Tosoh) disks of 50 mm of diameter are obtained by uniaxially pressing at 100 KN and a subsequent calcination at 1450 °C for 10 h. There is an intermediate sintering step at 1000 °C for 4 h to drill holes that facilitate the contact between wires and electrodes. Once the disk is fully dense, four rectangular-shaped working electrodes are screen-printed on one disk side, and one common cross-shape reference electrode is screen-printed on the back side. All of them are sintered at 1150 °C for 2 h (Figure 1). This new device provides flexibility as there is one common reference electrode catalytically active to oxygen and four channels to either test materials selective to C_2H_4 or check reproducibility of a selected electrode material.

Employing a LSM/8YSZ 50−50% mixture by volume as reference electrode instead of Pt should increase the triple phase boundary area. LSM provides electronic conductivity and activity toward O_2 activation, while 8YSZ provides the ionic conductivity. Therefore, there is an increase of the area where the electronical and ionic conductor meet the target gas, in this case O_2. Finally, a gold layer is screen printed and sintered at 900 °C for 2 h as current collector to ensure electrical conductivity in the whole surface. Silver paste is employed to ensure contact between electrode and wires. The porosity of the as-sintered gold layer remained open during the sensor testing (∼30 days) albeit grain morphology changes are observed.

Nickel and ruthenium nanoparticles were introduced into the working electrode by dropping a precursor solution (with the respective nitrates) on the surface of the sintered electrode by
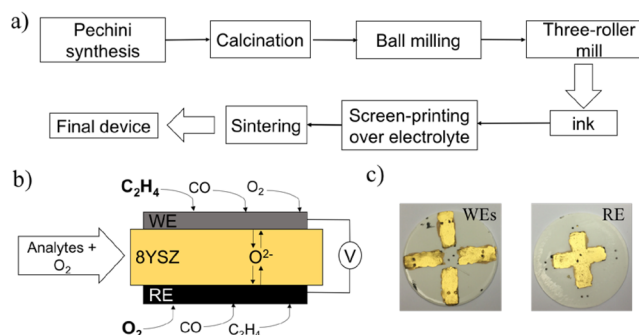
Figure 1. Schemes and camera pictures of the multidevice. (a) Scheme of the sensor fabrication procedure from the synthesis of the powder to the screen-printing of the layer into the electrolyte. (b) Cross-section schematics of the multisensor device showing the reactions that takes place at each electrode. Ideally, C_2H_4 anodic reaction controls the kinetics of the working electrode and O_2 cathodic reaction controls the kinetics of the reference electrode. The working electrode is infiltrated with Ni or Ru. (c) Top face with four $Fe_{0.7}Cr_{1.3}O_3$/8YSZ electrodes (channels) and individual gold layers as current collector; back face with LSM/8YSZ common reference electrode and a top common gold layer as current collector.

capillarity. The solution drenches the porous electrode filling up the pores. After drying of the impregnated electrode, a calcination step was followed in Ar at 550 °C for 4 h to remove the organic fraction. The device was then exposed to 5% H_2 in Ar at 550 °C for 4 h.

2.3. Sample Characterization. A PANalytical Cubix fast diffractometer, using Cu Kα1 radiation (λ = 1.5406 Å) and an X'Celerator detector in Bragg−Brentano geometry, was used for the identification of the crystalline phases. XRD patterns recorded in the 2θ range from 10° to 90° were analyzed using X'Pert Highscore Plus software. SEM and energy-dispersive X-ray spectroscopy (EDS) using a ZEISS Ultra55 field emission scanning electron microscope were used to analyze cross sections of the sintered material before and after the permeation test. SEM backscattered electrons detector (BSD) was used to provide images with compositional contrast that differentiates grains and element distribution.

The built cell voltage (so-called electromotive force, EMF) was determined by measuring the potential difference between the working and reference electrode when a zero ampere current is applied. Gold wires and silver paste were used for contacting electrodes. The measurements were carried out at 550 °C and under several concentrations of C_2H_4 and/or CO. The constant current was supplied by a programmable current source (Keithley 2601), and the voltage drop through the sample was detected by a multimeter (Keithley 3706). The response of the sensor (V_{cell}, mV) was defined as

$$V_{cell} = V_a - V_b \tag{1}$$

where V_a and V_b are the cell voltages of the sensor to analytes and to background gas of 6% O_2/Ar, respectively.

Mass flow controllers were used to mix the gases. The total gas flow rate was 550 mL/min with a 6% of oxygen, varying C_2H_4 and CO concentrations, and using argon as a balance. Once the sample is stabilized at 550 °C, the C_2H_4 or CO concentration was varied from 50 ppm (used as base gas) to 100, 150, and 200 ppm. The same test was performed for each analyte with 200 ppm of the other analyte as background in order to check the cross-sensitivity. Electrochemical impedance spectroscopy analysis was carried for each analyte at 200 ppm using an Autolab PGSTAT204 with a FRA32M module. The frequency was changed from 0.03 Hz to 1 MHz. Prior to the EIS measurement, open circuit voltage (OCV) is measured and this voltage is applied for the EIS measurement.

Surface analysis performed by X-ray photoelectron spectroscopy (XPS) was carried out on PHI Quantera equipment with a base pressure in the analysis chamber of 10^{-9} Torr. The X-ray source was

monochromatic Al Kα radiation (1486.6 eV), and the overall energy resolution is estimated at 0.65 eV by the full width at half-maximum (fwhm) of the Au $4f_{7/2}$ photoelectron line (84 eV). The charging effect was minimized by using a dual beam (electrons and Ar ions) as neutralizer, while the spectra were calibrated using the C 1s line (BE = 284.8 eV) of the adsorbed hydrocarbon on the sample surface (C−C and/or (CH)$_n$ bondings). As this spectrum was recorded at the start and the end of each experiment, the energy calibration during experiments was reliable. The metal surface area in the reduced catalyst was determined by H_2 chemisorption at 300 °C with a Quantachrome Autosorb-1C adsorption analyzer. Prior to adsorption the samples (∼0.5 g) were pretreated under flowing H_2 at 300 °C for 1 h.

3. RESULTS AND DISCUSSION

3.1. Microstructural Characterization. Analysis of the XRD patterns (Figure 2) for both materials confirms the
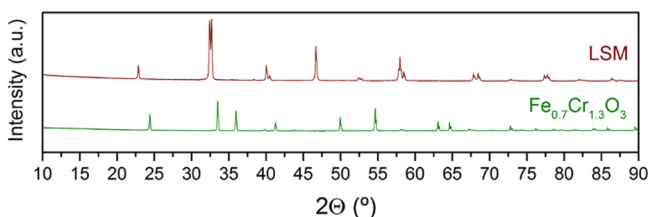
Figure 2. X-ray diffraction patterns of the as-sintered $Fe_{0.7}Cr_{1.3}O_3$ and LSM at room temperature.

formation of the desired phase for each material. The diffraction peaks corresponding to any other oxide or any precursor are not detected. The single phase $Fe_{0.7}Cr_{1.3}O_3$ is identified by XRD analysis where the peaks correspond to the cubic structure of the spinel. LSM phase is also confirmed by XRD analysis.

SEM analysis (Figure 3) shows the structural and morphologic characteristics of the built sensor device. The device consists of a 1.4 mm thick dense 8YSZ electrolyte, a ∼27 μm porous $Fe_{0.7}Cr_{1.3}O_3$/8YSZ working electrode with a gold layer (Figure 3c), and another porous layer of LSM/8YSZ with a thickness of ∼24 μm (Figure 3f). The cross section of the working electrode (from Figure 3a to Figure 3c) reveals a porous structure with a good distribution of $Fe_{0.7}Cr_{1.3}O_3$ and 8YSZ grains, although $Fe_{0.7}Cr_{1.3}O_3$ grains are bigger. Figure 3a

depicts the distribution and morphology of nickel nanoparticles after the functionalization of the electrode by infiltration. These nanoparticles are well distributed among the surface of the grains (Figure 3a). The reference LSM/8YSZ electrode (Figure 3d−f) presents homogeneous distribution of grains, while nickel particles are not detected; i.e., RE cross-contamination during infiltration of the WE is ruled out. No reaction interfaces are detected between electrodes and electrolyte. In addition, neither reaction between phases nor impurities on the grain boundaries are detected. Ruthenium nanoparticles are also well distributed in the working electrode (Figure S1).

Further studies were performed to confirm the oxidation state of nickel nanoparticles as nickel provided a better response than ruthenium. No further studies for ruthenium were performed as their results were less appealing than nickel. Fresh powder was prepared by impregnation with nickel and reduced at 300 °C in H_2. First, a H atom chemisorption was done to check the adsorption of H_2 on nickel. This analysis indicates that there is a metallic active surface area of 3.15 × 10^{-2} m^2/g. In addition, XPS analysis was performed on the working electrode after sensor testing as well as on the fresh powder with nickel impregnated and reduced at 300 °C. After the deconvolution of the Ni $2p_{3/2}$ XPS spectra (Figure 4), three contributions related to metallic Ni and Ni oxides[35−38] can be observed. After potentiometric sensor characterization, nickel nanoparticles are partially reoxidized, as the metallic nickel contribution is less than in the case of the H_2-reduced sample. Note that the sensor electrode is not subjected to any reduction treatment in H_2 prior to the potentiometric test in CO/C_2H_4 at 550 °C. These results combined with the H atom chemisorption and the potentiometric measurements confirm that metallic nickel is partially present in the working electrode.

3.2. Electrochemical Characterization. Several oxidation and reduction reactions take place at the interface among electrode, electrolyte and gas, in the presence of reducing agents (e.g., CO, hydrocarbons) and O_2. As the reaction takes place at the triple phase boundary (TPB), the electrodes must be porous to favor analyte diffusion through the electrode into the contact point with electronic and ionic conductors. In each electrode one of the reactions will control the kinetics. When equilibrium is achieved, the oxidation of the reducing agent in the working electrode (eqs 3 and 4) occurs while, in the other
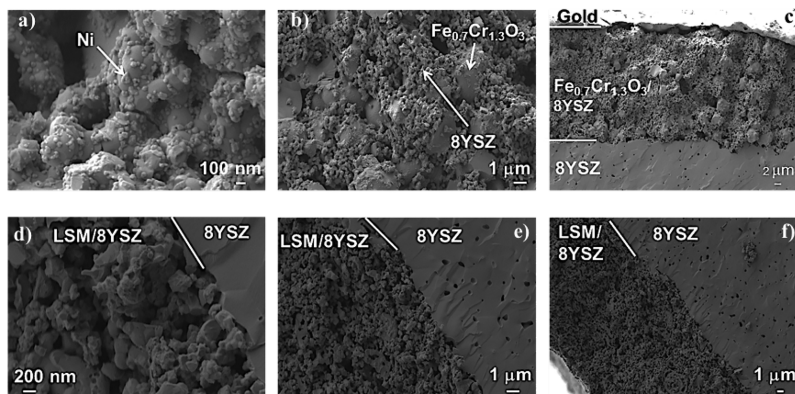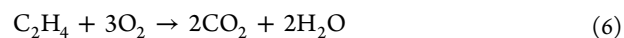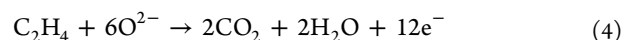

Figure 3. SEM image of the device cross-section corresponding to $Fe_{0.7}Cr_{1.3}O_3$/8YSZ as WE and LSM/8YSZ as RE: (a) WE electrode cross section with $Fe_{0.7}Cr_{1.3}O_3$/8YSZ grains covered by nanosized nickel particles; (b) WE electrode cross section with $Fe_{0.7}Cr_{1.3}O_3$/8YSZ grains distribution; (c) interface WE-electrolyte, where gold collector layer at top can be observed; (d) RE electrode cross section with LSM and 8YSZ grains; (e) RE electrode cross section with LSM and 8YSZ grains distribution; (f) interface RE-electrolyte.
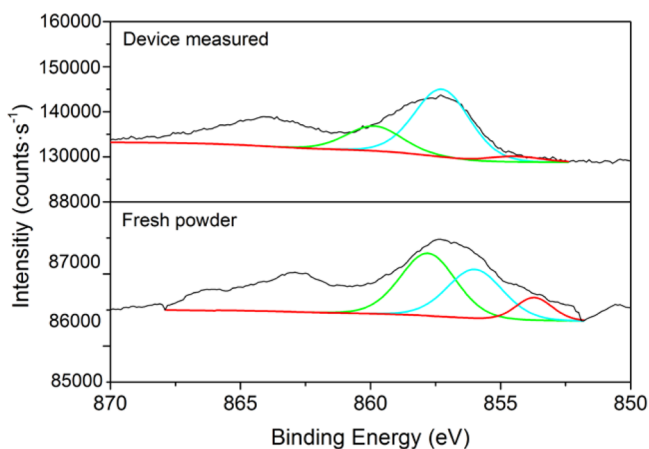
Figure 4. Ni 2p3/2 XPS deconvoluted spectra for the working electrode of the device after potentiometric measurement (top) and for fresh powder impregnated with nickel (bottom). There are three contributions: Ni (red) and Ni oxides (cyan and green).
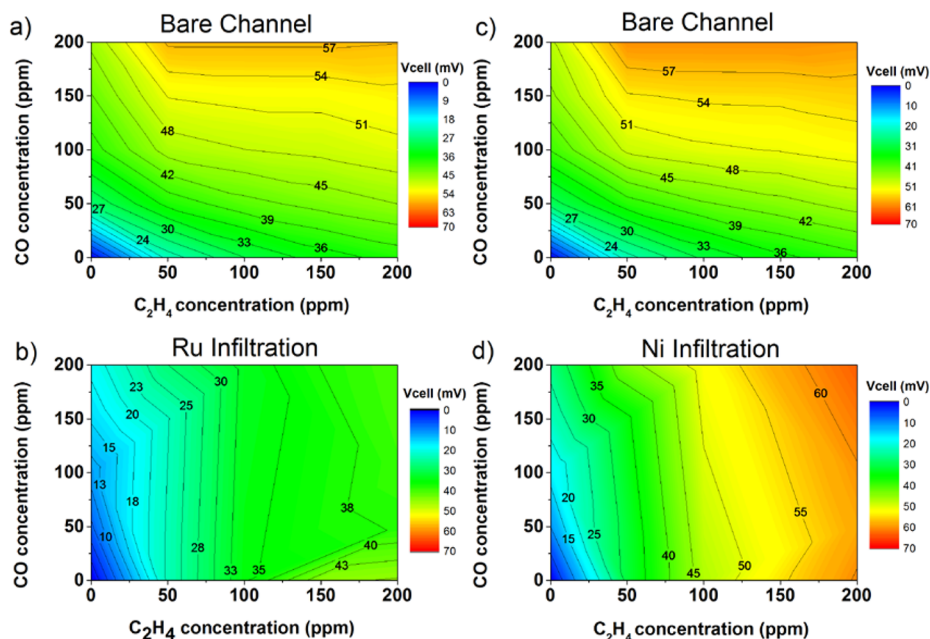
$$\frac{1}{2}O_2 + 2e^- \rightarrow O^{2-} \tag{2}$$

$$CO + O^{2-} \rightarrow CO_2 + 2e^- \tag{3}$$

$$C_2H_4 + 6O^{2-} \rightarrow 2CO_2 + 2H_2O + 12e^- \tag{4}$$

$$CO + 0.5O_2 \rightarrow CO_2 \tag{5}$$

$$C_2H_4 + 3O_2 \rightarrow 2CO_2 + 2H_2O \tag{6}$$

The objective of this work is to develop a device employing LSM/8YSZ as reference electrode with a selective response to C_2H_4 and a low cross-sensitivity toward CO. The sensor should be optimized to provide low cross-sensitivity toward water as it has a negative effect on the sensor response.

Unfortunately, when the sensor is exposed to C_2H_4 and CO, an unexpected sensor response is observed (Figure 5a and Figure 5b). Despite the active reference electrode to oxygen, the sensor response is not selective to C_2H_4 and the cross-sensitivity toward CO is too high. The change in response with C_2H_4 concentration is lower than to CO. Moreover, the addition of 200 ppm of CO as background disables the sensor response to C_2H_4 as the main contribution is due to CO. However, the reproducibility of the device can be confirmed as both devices provide the same response.

Therefore, the catalytic activity of the working electrode to C_2H_4 should be improved; i.e., C_2H_4 selectivity should be raised. Surface catalytic activation of the working electrode is performed by nickel and ruthenium nanoparticles deposition. Both metals are selected because of their catalytic activity for oxidation of hydrocarbons and CO.[31−34,44] The working electrode material of each device, $Fe_{0.7}Cr_{1.3}O_3$/8YSZ composite, is infiltrated with a ruthenium 0.13 M aqueous solution in the first channel and with a nickel 0.5 M aqueous solution in the second channel. The solution is dropped on the surface of the sintered electrode, and it fills the pores of the electrode by

electrode, O_2 is reduced to form oxide-ions (eq 2). Cathodic and anodic reactions are coupled by the oxide-ion diffusion through the 8YSZ electrolyte. Therefore, according to mixed potential theory, the sensor response is controlled by kinetics in this case.[39−43] In the potentiometric sensor, a zero-current is imposed. When the steady state between the anodic reaction (eq 3 or 4) and the cathodic reaction (eq 2) is reached, a mixed-potential is established. The difference between the built mixed-potential in both electrodes is the final cell voltage. Heterogeneous catalytic conversion in the WE of the target gases (analytes) with locally adsorbed O_2 can occur at the same time and could be more favored than the electrochemical reaction. Since there is a competition between both mechanisms, these reactions (eq 5 and 6) should be also taken into account.

Figure 5. Sensor response (cell voltage) as a function of analyte concentration for (a) channel 1 as screen-printed, with $Fe_{0.7}Cr_{1.3}O_3$/8YSZ as WE and LSM/8YSZ as RE; (b) channel 1 with $Fe_{0.7}Cr_{1.3}O_3$/8YSZ infiltrated with Ru; (c) channel 2 as screen-printed, with $Fe_{0.7}Cr_{1.3}O_3$/8YSZ as WE and LSM/8YSZ as RE; (d) channel 2 with $Fe_{0.7}Cr_{1.3}O_3$/8YSZ infiltrated with Ni.

capillarity. After drying and later calcination at 550 °C for 4 h in argon, and an additional treatment for 4 h at 550 °C in hydrogen, the metallic nanoparticles are formed.

After infiltration, both Ru- and Ni-infiltrated sensors exhibit similar sensor behavior with respect to the pristine electrode. An increase in the sensor response to C_2H_4 can be observed in Figure 5b and Figure 5d for Ru and Ni infiltration respectively when compared to the bare sensor response (Figure 5a and Figure 5c). The change in response with C_2H_4 concentration is higher than to CO. Moreover, the effect of CO on C_2H_4 response is negligible; i.e., the addition of CO as background has no effect on the sensor response to C_2H_4 (Figure 6b),
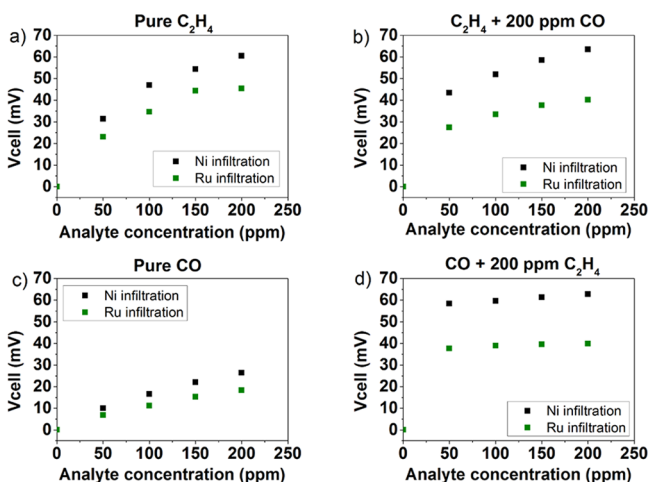
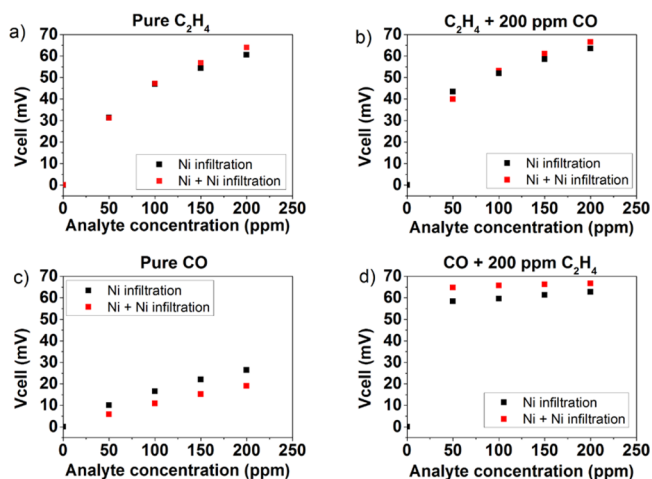
Figure 6. Response (cell voltage) of the sensor infiltrated with nickel (black) and ruthenium (blue) as a function of analyte concentration: (a) C_2H_4 changes in concentration; (b) C_2H_4 changes in concentration with 200 ppm of CO as background; (c) CO changes in concentration; (d) CO changes in concentration with 200 ppm of C_2H_4 as background.

while the addition of 200 ppm of C_2H_4 background determines the sensor response (Figure 6d). Therefore, the deposition of nickel and ruthenium nanoparticles onto the working electrode gives rise to a sensor selective to C_2H_4 with low cross-sensitivity toward CO in dry conditions. Electrode infiltration promotes preferentially the electrochemical reaction to ethylene, and this affects the equilibrium achieved in the working electrode and therefore leads to changes in the sensor response. This can explain the improvement in the sensor performance in terms of response to ethylene and output voltage when compared to the bare sensor.

Although both infiltrations show a similar response, Ni addition provides a better performance. Figure 6a and Figure 6b reveal that not only the response to C_2H_4 is higher for Ni-loaded cell but also the slope-linear change in response with analyte concentration. This can be attributed to a better selectivity to C_2H_4 of Ni over Ru. The lower performance of Ru-infiltrated electrodes should not be attributed to poor dispersion of nanoparticles, as inferred from SEM analysis in the working electrode. Therefore, the better performance of Ni-infiltrated sensors could be related to the better intrinsic catalytic properties of Ni nanoparticles that boost anodic (oxidation reactions) in WE at the working atmosphere at 550 °C. Moreover, the addition of the nanocatalyst could also promote the CO heterogeneous catalyst reaction. Thus, the amount of CO available for the electrochemical reaction is

decreased, and this may reduce the sensor cross-sensitivity toward CO.

A second infiltration with Ni is performed to check if further improvement of the catalytic activity to C_2H_4 could be achieved. Figure 7a and Figure 7b show that the response to


Figure 7. Response (cell voltage) of the sensor with nickel (black) and nickel twice (red) as a function of analyte concentration: (a) C_2H_4; (b) C_2H_4 with 200 ppm background of CO; (c) CO; (d) CO with 200 ppm background of C_2H_4.

C_2H_4 remains practically equal after the second infiltration in terms of absolute value and slope (change in response with analyte concentration) for pure C_2H_4 as well as when 200 ppm of CO is added. However, there is a change in the response to CO as can be observed in Figure 7c and Figure 7d, as an additional infiltration with nickel leads to a further decrease of the slope. This means that the change in concentration with CO concentration is less for the second infiltration. Moreover, the response of the twice-infiltrated sensor depends completely on the C_2H_4 concentration when 200 ppm of C_2H_4 is added. Therefore, a second infiltration with nickel improves the sensor performance. Although the sensor response to C_2H_4 remains constant, the CO response decreases; i.e., the cross-sensitivity toward CO is lower.

The device shows good reproducibility and stability as can be inferred from Figure 8 where the V_{cell} transient response is depicted for changes in concentration of C_2H_4 and CO in the 50−200 ppm range for both analytes individually as well as with a background of 200 ppm of the other analyte. The Ni-infiltrated sensor response is stable for each analyte concentration cycle (after a certain stabilization time), and the absolute value achieved for 50 ppm is constant.

Regarding NO_2 cross-sensitivity on the RE, LSM/8YSZ is well-known for its catalytic activity toward O_2 at mid-high temperatures. NO_2 is a common compound in a diesel exhaust gas and could compromise the equilibrium achieved at the reference electrode for oxygen reduction. This is confirmed by Figure S2a as the sensor works upside-down when is exposed to concentrations pulses of NO_2 from 50 to 200 ppm. (Note that neither C_2H_4 nor CO is added to the gas.) Reduction of NO_2 is taking place at the reference electrode. However, according to similar potentiometric sensors, NO_2 is not expected to affect the reference electrode performance or the overall sensor response.[45−49]
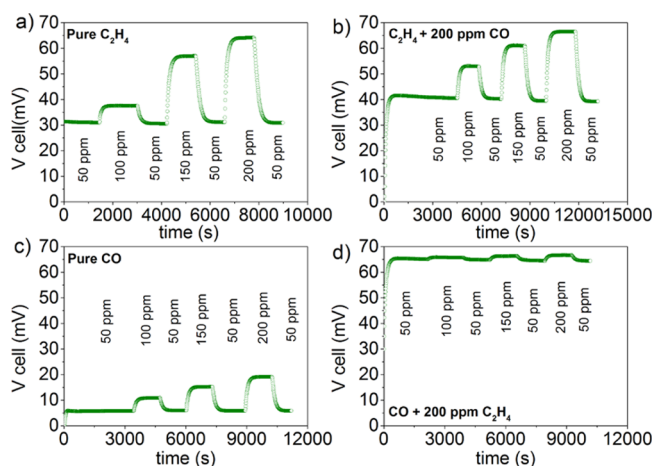
Figure 8. Response curves for changes in concentration of (a) C_2H_4, (b) C_2H_4 with a background of 200 ppm of CO, (c) CO, and (d) CO with a background of 200 ppm of C_2H_4. Each change in concentration has 20 min of duration, and they are performed in the range 50–200 ppm.

Figure S2b shows the normalized sensor response to C_2H_4 when there is only C_2H_4 as well as when a background of 200 ppm of CO or NO_2 is added. Thus, there is certain cross-sensitivity toward NO_2, but the sensor response is still controlled by C_2H_4 concentration.

In order to shed further light into these electrochemical results, electrochemical impedance spectroscopy (EIS) analysis is performed for 200 ppm of pure CO and C_2H_4.

EIS analysis provides information about the different processes occurring in sensor (ion transport, solid−solid interfacial resistance, gas−solid surface reactions) since each process presents distinct characteristic frequencies. Changes in the type of analyte concentration may principally affect the impedance contributions linked to gas−solid surface reactions and appearing at the lowest frequencies. The larger the impedance, the slower the kinetics of the specific surface reaction (e.g., oxidation of analytes) is.

The analysis was carried out for the following sensor channels: as-sintered (bare) electrode, after infiltration with Ni, and after second infiltration with Ni. The Nyquist plots (0.03 Hz to 1 MHz range) are depicted in Figure 9. The EIS spectra can be fitted to an equivalent circuit consisting of two parallel combinations of resistance-constant phase element (R-CPE) circuits connected in series (Figure 9b, inlet). The shape of the arc at high frequencies is similar in all cases. The first arc

contribution ($C = 10^{-5}-10^{-6}$ F) at 550 °C can be attributed to the interface between the electrodes and the 8YSZ electrolyte (Figure 9a, Table S1). $R_{interface}$ values are similar for both analytes in every condition (Table S1), and consequently the ionic mobility remains almost unaffected. Regarding the $R_{electrode}$, the sensor with the as-sintered bare WE presents a similar value for both analytes (Table S1). This is in agreement with the lack of selectivity to C_2H_4 and high cross-sensitivity toward CO observed in Figure 5a and Figure 5c. Otherwise, infiltration with Ni leads to differentiated arc contributions for C_2H_4 and CO (Table S1). Thus, this indicates that there is a modification of the surface activity and the kinetics of the catalytic processes occurring on the electrodes. CO contribution is increased considerably, while the C_2H_4 contribution remains almost constant (Figure 9 and Table S1). The second infiltration with Ni enables the reduction of both C_2H_4 and CO contributions (Figure 9 and Table S1). After infiltration, there is a significant difference in the polarization resistance (R_p) between C_2H_4 and CO conditions (Table S1). This can explain the selective sensor response to C_2H_4 with a low cross-sensitivity toward CO. The nanocatalyst addition changes the equilibrium achieved in the working electrode, and therefore it modifies the device behavior. CO oxidation exhibits higher resistance and therefore is more restricted than C_2H_4, in line with the potentiometric results.

The effect of the sensor operation under moist conditions was studied by exposing the twice Ni-infiltrated WE to gas environments with 3% (by vol) of water. According to previous studies, the influence of water on the signal response is detrimental; i.e., water presence leads to higher sensor response for both analytes as well as to an increment of the CO cross-sensitivity.[23,26] Figure 10a depicts the normalized response under wet conditions of an individual sensor with the same configuration but with platinum as RE. On the other hand, Figure 10b depicts the response under wet conditions of the current multidevice with LSM/8YSZ as RE. Figure 10a reveals that the device with platinum as RE has poor selectivity to C_2H_4 under wet conditions. In contrast, the device developed here exhibits selective response to C_2H_4 and low CO cross-sensitivity in wet conditions (Figure 10b) albeit CO influence is higher than in dry conditions. In summary, Ni infiltration enables us to selectively sense C_2H_4 with low cross-sensitivity in dry as well as in wet conditions. However, an optimization of the device through miniaturization is required for final application and testing in demanding real conditions, in order to have a fast-enough response for on-board diagnosis of real exhaust gas.
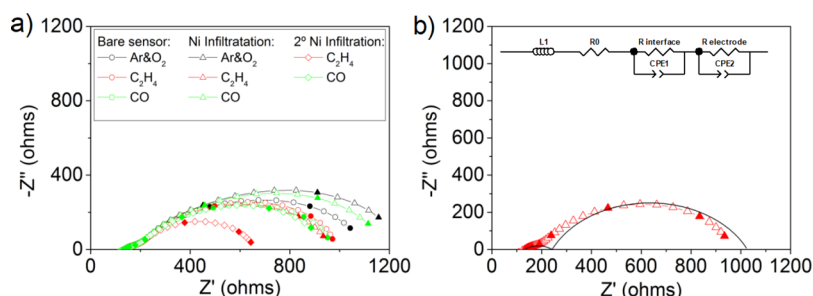
Figure 9. (a) Impedance spectrometry study for screen-printed device (open circle), infiltrated with nickel (open triangle) and twice-infiltrated with nickel (empty rhomb dot). Nyquist plot is depicted for Ar + 6% O_2 base gas (black), 200 ppm of C_2H_4 (red), and 200 ppm of CO (green). (b) Example of EIS fitting to an equivalent circuit consisting of two parallel combinations of resistance-constant phase element (R-CPE) for 200 ppm of C_2H_4 of the bare sensor.
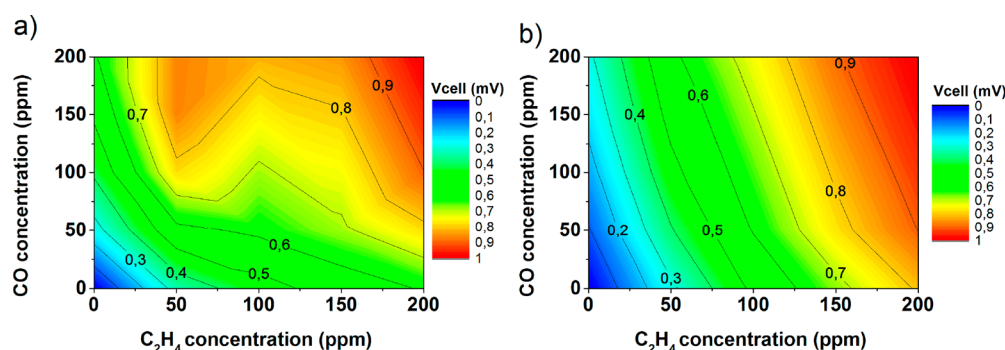
Figure 10. Sensor response (cell voltage) in wet conditions (3% H_2O) as a function of analytes concentration for (a) previous sensor reported consisting of $Fe_{0.7}Cr_{1.3}O_3/8YSZ//8YSZ//Pt$ and (b) device consisting of $Fe_{0.7}Cr_{1.3}O_3/8YSZ//8YSZ//LSM/8YSZ$ where $Fe_{0.7}Cr_{1.3}O_3/8YSZ$ is infiltrated with Ni twice.

4. CONCLUSIONS

The development of a mixed-potential-based electrochemical cell for selective C_2H_4 sensing is reported. The sensor cell comprises a disk-shaped solid oxide-ion conducting electrolyte (8YSZ) coated with four working electrodes ($Fe_{0.7}Cr_{1.3}O_3/8YSZ$) and a common reference electrode (LSM/8YSZ) on the other side. This new reference electrode provides an inexpensive alternative to state-of-the-art Pt electrodes. The catalytic activity of the working electrode was improved through catalytic surface activation by nickel nanoparticle deposition. The addition of the nanoparticles boosts the electrochemically driven oxidation to C_2H_4 while it has a lesser effect on CO oxidation, as inferred by impedance spectroscopy analysis. The study using wet gas environments reveals selective sensor response to C_2H_4 with low cross-sensitivity toward CO, and this makes this sensor suitable for application in conditions like exhaust gases from diesel cars. Furthermore, the proposed four channels design can be used either to detect several species modifying the WE or to study the reproducibility.

ASSOCIATED CONTENT

Ⓢ Supporting Information

The Supporting Information is available free of charge on the ACS Publications website at DOI: 10.1021/acsanm.8b01486.

> FESEM image of the WE electrode cross section with $Fe_{0.7}Cr_{1.3}O_3/8YSZ$ grains covered by ruthenium nanoparticles; sensor response curve for changes in concentration of NO_2 from 50 to 200 ppm as well as C_2H_4 concentration pulses from 50 to 200 ppm for pure C_2H_4, with 200 ppm of background CO and with 200 ppm of background NO_2; list of results obtained by fitting the impedance data to the equivalent circuit in Figure 5b (PDF)

AUTHOR INFORMATION

Corresponding Author

*E-mail: jmserra@itq.upv.es.

ORCID Ⓞ

J. M. Serra: 0000-0002-1515-1106

Notes

The authors declare no competing financial interest.

REFERENCES

(1) Krzyzanowski, M.; Kuna-Dibbert, B.; Schneider, J. *Health Effects of Transport-Related Air Pollution*; World Health Organization Regional Office for Europe: Copenhagen, Denmark, 2005.

(2) www.dieselnet.com/standards/eu/ld.php#stds (accessed Jun 28, 2018).

(3) Sekhar, P. K.; Subramaniyam, K. Electrical Characterization of a Mixed Potential Propylene Sensor. *Sens. Actuators, B* **2013**, *188*, 367−371.

(4) Reşitoğlu, İ. A.; Altinişik, K.; Keskin, A. The Pollutant Emissions from Diesel-Engine Vehicles and Exhaust Aftertreatment Systems. *Clean Technol. Environ. Policy* **2015**, *17*, 15−27.

(5) McCulloch, M. T.; Langford, N.; Duxbury, G. Real-Time Trace-Level Detection of Carbon Dioxide and Ethylene in Car Exhaust Gases. *Appl. Opt.* **2005**, *44*, 2887−2894.

(6) Grosjean, E.; Rasmussen, R. A.; Grosjean, D. Ambient Levels of Gas Phase Pollutants in Porto Alegre, Brazil. *Atmos. Environ.* **1998**, *32*, 3371−3379.

(7) Poulopoulos, S. G.; Samaras, D. P.; Philippopoulos, C. J. Regulated and Unregulated Emissions from an Internal Combustion Engine Operating on Ethanol-Containing Fuels. *Atmos. Environ.* **2001**, *35*, 4399−4406.

(8) Storey, J. M.; Lewis, S. A.; West, B. H.; Huff, S. P.; Sluder, C. S.; Wagner, M. R.; Domingo, N.; Thomas, J.; Kass, M. Hydrocarbon species in the exhaust of diesel engines equipped with advanced emissions control devices. Final Report CRC Project No. AVFL-10b-2; Oak Ridge National Laboratory: Oak Ridge, TN, 2005.

(9) Brosha, E. L.; Mukundan, R.; Brown, D. R.; Garzon, F. H.; Visser, J. H.; Zanini, M.; Zhou, Z.; Logothetis, E. M. CO/HC Sensors Based on Thin Films of LaCoO3 and La0.8Sr0.2CoO3 Metal Oxides. *Sens. Actuators, B* **2000**, *69*, 171−182.

(10) Chevallier, L.; Dibartolomeo, E.; Grilli, M.; Traversa, E. High Temperature Detection of CO/HCs Gases by Non-Nernstian Planar Sensors Using Nb2O5 Electrode. *Sens. Actuators, B* **2008**, *130*, 514−519.

(11) Liu, F.; Wang, B.; Yang, X.; Guan, Y.; Sun, R.; Wang, Q.; Liang, X.; Sun, P.; Lu, G. High-Temperature Stabilized Zirconia-Based Sensors Utilizing MNb2O6 (M: Co, Ni and Zn) Sensing Electrodes for Detection of NO2. *Sens. Actuators, B* **2016**, *232*, 523−530.

(12) Sekhar, P. K.; Kysar, J.; Brosha, E. L.; Kreller, C. R. Development and Testing of an Electrochemical Methane Sensor. *Sens. Actuators, B* **2016**, *228*, 162−167.

(13) Fadeyev, G.; Kalakin, A.; Demin, A.; Volkov, A.; Brouzgou, A.; Tsiakaras, P. Electrodes for Solid Electrolyte Sensors for the

Measurement of CO and H2 Content in Air. *Int. J. Hydrogen Energy* **2013**, *38*, 13484−13490.

(14) Fergus, J. W. Perovskite Oxides for Semiconductor-Based Gas Sensors. *Sens. Actuators, B* **2007**, *123*, 1169−1179.

(15) Romanytsia, I.; Viricelle, J. P.; Vernoux, P.; Pijolat, C. Application of Advanced Morphology Au-X (X = YSZ, ZrO2) Composites as Sensing Electrode for Solid State Mixed-Potential Exhaust NOx Sensor. *Sens. Actuators, B* **2015**, *207*, 391−397.

(16) Yamaguchi, M.; Anggraini, S. A.; Fujio, Y.; Sato, T.; Breedon, M.; Miura, N. Stabilized Zirconia-Based Sensor Utilizing SnO2-Based Sensing Electrode with an Integrated Cr2O3 Catalyst Layer for Sensitive and Selective Detection of Hydrogen. *Int. J. Hydrogen Energy* **2013**, *38*, 305−312.

(17) Macam, E. R.; White, B. M.; Blackburn, B. M.; Di Bartolomeo, E.; Traversa, E.; Wachsman, E. D. La2CuO4 Sensing Electrode Configuration Influence on Sensitivity and Selectivity for a Multi-functional Potentiometric Gas Sensor. *Sens. Actuators, B* **2011**, *160*, 957−963.

(18) Fujio, Y.; Sato, T.; Miura, N. Sensing Performance of Zirconia-Based Gas Sensor Using Titania Sensing-Electrode Added with Palladium. *Solid State Ionics* **2014**, *262*, 266−269.

(19) Zosel, J.; Müller, R.; Vashook, V.; Guth, U. Response Behavior of Perovskites and Au/Oxide Composites as HC-Electrodes in Different Combustibles. *Solid State Ionics* **2004**, *175*, 531−533.

(20) Mori, M.; Sadaoka, Y.; Nakagawa, S.; Kida, M.; Kojima, T. Development of Ethanol and Toluene Sensing Devices with a Planar-Type Structure Based on YSZ and Modified Pt Electrodes. *Sens. Actuators, B* **2013**, *187*, 509−513.

(21) Elumalai, P.; Plashnitsa, V. V.; Fujio, Y.; Miura, N. Highly Sensitive and Selective Stabilized Zirconia-Based Mixed-Potential-Type Propene Sensor Using NiO/Au Composite Sensing-Electrode. *Sens. Actuators, B* **2010**, *144*, 215−219.

(22) Li, Y.; Li, X.; Tang, Z.; Wang, J.; Yu, J.; Tang, Z. Potentiometric Hydrogen Sensors Based on Yttria-Stabilized Zirconia Electrolyte (YSZ) and CdWO4 Interface. *Sens. Actuators, B* **2016**, *223*, 365−371.

(23) Toldra-Reig, F.; Serra, J. M. Development of Potentiometric Sensors for C2H4 Detection. *Sensors* **2018**, *18*, 2992.

(24) Plashnitsa, V. V.; Elumalai, P.; Fujio, Y.; Miura, N. Zirconia-Based Electrochemical Gas Sensors Using Nano-Structured Sensing Materials Aiming at Detection of Automotive Exhausts. *Electrochim. Acta* **2009**, *54*, 6099−6106.

(25) Zhang, X.; Kohler, H.; Schwotzer, M.; Guth, U. Mixed-Potential Gas Sensor with PtAu-8YSZ Sensing Electrode: Electric Potential Difference Measurements at Isothermal and Thermo-Cyclic Operation. *Sens. Actuators, B* **2015**, *217*, 107−112.

(26) Navarrete, L.; Toldra-Reig, F.; Serra, J. M.; Somacescu, S. SnO2 and Ce Modified SnO2 Mesostructured for Selective Ethanol Detection. *Sensors, 2014 IEEE* **2014**, 297−300.

(27) Fergus, J. W. Sensing Mechanism of Non-Equilibrium Solid-Electrolyte-Based Chemical Sensors. *J. Solid State Electrochem.* **2011**, *15*, 971−984.

(28) Iio, A.; Ikeda, H.; Anggraini, S. A.; Miura, N. Potentiometric YSZ-Based Oxygen Sensor Using BaFeO3 Sensing-Electrode. *Electrochem. Commun.* **2014**, *48*, 134−137.

(29) Kuhn, M.; Napporn, T. W.; Meunier, M.; Therriault, D. Single-Chamber Micro Solid Oxide Fuel Cells: Study of Anode and Cathode Materials in Coplanar Electrode Design. *Solid State Ionics* **2010**, *181*, 332−337.

(30) Morel, B.; Roberge, R.; Savoie, S.; Napporn, T. W.; Meunier, M. Catalytic Activity and Performance of LSM Cathode Materials in Single Chamber SOFC. *Appl. Catal., A* **2007**, *323*, 181−187.

(31) Ghosh, A.; Kumari, N.; Tewari, S.; Bhattacharjee, A. Structural, Electrical and Optical Studies on Ruthenium Doped ZnO Pellets for Device Applications. *Mater. Sci. Eng., B* **2015**, *196*, 7−14.

(32) Monteiro, N. K.; Noronha, F. B.; Da Costa, L. O. O.; Linardi, M.; Fonseca, F. C. A Direct Ethanol Anode for Solid Oxide Fuel Cell Based on a Chromite-Manganite with Catalytic Ruthenium Nano-particles. *Int. J. Hydrogen Energy* **2012**, *37*, 9816−9829.

(33) Niranjan, R. S.; Sainkar, S. R.; Vijayamohanan, K.; Mulla, I. S. Ruthenium: Tin Oxide Thin Film as a Highly Selective Hydrocarbon Sensor. *Sens. Actuators, B* **2002**, *82*, 82−88.

(34) Karczewski, J.; Bochentyn, B.; Molin, S.; Gazda, M.; Jasinski, P.; Kusz, B. Solid Oxide Fuel Cells with Ni-Infiltrated Perovskite Anode. *Solid State Ionics* **2012**, *221*, 11−14.

(35) Grosvenor, A. P.; Biesinger, M. C.; Smart, R. S. C.; McIntyre, N. S. New Interpretations of XPS Spectra of Nickel Metal and Oxides. *Surf. Sci.* **2006**, *600*, 1771−1779.

(36) Hagelin-Weaver, H. A. E.; Weaver, J. F.; Hoflund, G. B.; Salaita, G. N. Electron Energy Loss Spectroscopic Investigation of Ni Metal and NiO before and after Surface Reduction by Ar+ Bombardment. *J. Electron Spectrosc. Relat. Phenom.* **2004**, *134*, 139−171.

(37) Prieto, P.; Nistor, V.; Nouneh, K.; Oyama, M.; Abd-Lefdil, M.; Diaz, R. XPS Study of Silver, Nickel and Bimetallic Silver−Nickel Nanoparticles Prepared by Seed-Mediated Growth. *Appl. Surf. Sci.* **2012**, *258*, 8807−8813.

(38) Solís, C.; Somacescu, S.; Palafox, E.; Balaguer, M.; Serra, J. M. Particular Transport Properties of NiFe2O4 Thin Films at High Temperatures. *J. Phys. Chem. C* **2014**, *118*, 24266−24273.

(39) Di Bartolomeo, E.; Grilli, M. L.; Traversa, E. Sensing Mechanism of Potentiometric Gas Sensors Based on Stabilized Zirconia with Oxide Electrodes. *J. Electrochem. Soc.* **2004**, *151*, H133−H139.

(40) Park, C. O.; Fergus, J. W.; Miura, N.; Park, J.; Choi, A. Solid-State Electrochemical Gas Sensors. *Ionics* **2009**, *15*, 261−284.

(41) Miura, N.; Sato, T.; Anggraini, S. A.; Ikeda, H.; Zhuiykov, S. A Review of Mixed-Potential Type Zirconia-Based Gas Sensors. *Ionics* **2014**, *20*, 901−925.

(42) Miura, N.; Raisen, T.; Lu, G.; Yamazoe, N. Highly Selective CO Sensor Using Stabilized Zirconia and a Couple of Oxide Electrodes. *Sens. Actuators, B* **1998**, *47*, 84−91.

(43) Garzon, F. H.; Mukundan, R.; Brosha, E. L. Solid-State Mixed Potential Gas Sensors: Theory, Experiments and Challenges. *Solid State Ionics* **2000**, *136−137*, 633−638.

(44) Makgwane, P. R.; Ray, S. S. Nanosized Ruthenium Particles Decorated Carbon Nanofibers as Active Catalysts for the Oxidation of P-Cymene by Molecular Oxygen. *J. Mol. Catal. A: Chem.* **2013**, *373*, 1−11.

(45) Pal, N.; Murray, E. P. Dense LaSrMnO 3 Composite Electrodes for NO x Sensing. *Sens. Actuators, B* **2018**, *256*, 351−358.

(46) Morata, A.; Viricelle, J. P.; Tarancón, A.; Dezanneau, G.; Pijolat, C.; Peiro, F.; Morante, J. R. Development and Character-isation of a Screen-Printed Mixed Potential Gas Sensor. *Sens. Actuators, B* **2008**, *130*, 561−566.

(47) Zou, J.; Zheng, Y.; Li, J.; Zhan, Z.; Jian, J. Potentiometric NO2 Sensors Based on Thin Stabilized Zirconia Electrolytes and Asymmetric (La0.8Sr0.2)0.95MnO3 Electrodes. *Sensors* **2015**, *15*, 17558−17571.

(48) Reinhardt, G.; Wiemhöfer, H.-D.; Göpel, W. Electrode Reactions of La$_{0.8}$Sr$_{0.2}$MnO$_{3\pm\delta}$-Electrodes on Stabilized Zirconia with Oxygen and the Nitrogen Oxides NO and NO$_2$. *Ionics* **1995**, *1*, 32−39.

(49) Woo, L. Y.; Glass, R. S. NOx Sensor Development. Propulsion Materials FY 2008 Progress Report; Lawrence Livermore National Laboratory, 2009.